Energy storage properties of ferroelectric nanocomposites

Zhijun Jiang,[1,*] Zhenlong Zhang,[1] Sergei Prokhorenko,[2] Yousra Nahas,[2] Sergey Prosandeev,[2] and Laurent Bellaiche[2,†]

[1]*MOE Key Laboratory for Nonequilibrium Synthesis and Modulation of Condensed Matter, School of Physics, Xi'an Jiaotong University, Xi'an 710049, China*

[2]*Physics Department and Institute for Nanoscience and Engineering, University of Arkansas, Fayetteville, Arkansas 72701, USA*

(Received 13 March 2023; revised 23 May 2023; accepted 8 June 2023; published 20 June 2023)

An atomistic effective Hamiltonian technique is used to investigate the finite-temperature energy storage properties of a ferroelectric nanocomposite consisting of an array of $BaTiO_3$ nanowires embedded in a $SrTiO_3$ matrix, for electric field applied along the long axis of the nanowires. We find that the energy density versus temperature curve adopts a nonlinear, mostly temperature-independent response when the system exhibits phases possessing an out-of-plane polarization and vortices, while the energy density more linearly increases with temperature when the nanocomposite either only possesses vortices (and thus no spontaneous polarization) or is in a paraelectric and paratoroidic phase for its equilibrium state. Ultrahigh-energy density up to $\simeq$141 J/cm^3 and an ideal 100% efficiency are also predicted in this nanocomposite. A phenomenological model, involving a coupling between polarization and toroidal moment, is further proposed to interpret these energy density results.

DOI: 10.1103/PhysRevB.107.214105

I. INTRODUCTION

Dielectric capacitors with high-energy densities and efficiencies are particularly promising for advanced electronics and electric power systems due to their ultrafast charging/discharging rates [1–5]. However, traditional commercial dielectric capacitors, such as biaxially oriented polypropylene, possess relatively low energy density of about 1.2 J/cm^3 [6] while intensive works have been devoted to improve their energy densities and efficiencies. One key parameter for energy storage is the recoverable energy density, which is defined as $U = \int_{P_r}^{P_{max}} \mathcal{E} dP$ [4], where P_{max} is the maximum polarization at the maximal applied field, $\mathcal{E}_{max}$, and P_r is the remnant polarization under zero electric field. Another key parameter is the efficiency η, defined as $\eta = [U/(U + U_{loss})] \times 100\%$ [4], where U_{loss} is the dissipated energy because of hysteresis loss and is associated with the area inside the polarization-versus-electric field (P-$\mathcal{E}$) hysteresis loop.

In the last decade, ferroelectric thin films, dielectrics, antiferroelectrics, relaxor ferroelectrics, superlattices, and lead-free paraelectrics have been intensively studied in the search of large energy densities and efficiencies [7–17]. For instance, an ultrahigh-energy density of 112 J/cm^3 with a high-energy efficiency of 80% has been observed in lead-free ferroelectric $BiFeO_3$-$BaTiO_3$-$SrTiO_3$ films [7]. For antiferroelectrics, a giant energy density of 154 J/cm^3 and 97% efficiency has been achieved in epitaxial lead-free thin films [8]. Moreover, relaxor ferroelectrics can also possess ultrahigh-energy densities up to 156 J/cm^3 and efficiencies above 90% [11–14]. Epitaxial and initially nonpolar AlN/ScN superlattices have also been predicted to have ultrahigh-energy densities up to 200 J/cm^3 with an ideal efficiency of 100% [16].

Furthermore, ferroelectric nanocomposites combining ceramic filler and polymer matrix have shown great potential for high-energy storage capacitors because of their high breakdown strength and high dielectric permittivity [18–20]. Experimentally, nanocomposites made of $Ba_{0.2}Sr_{0.8}TiO_3$ nanowires were shown to reach a high-energy density of 14.86 J/cm^3 at 4.5×10^8 V/m. Based on phase field calculations, Liu *et al.* also numerically found an energy density of 5 J/cm^3 and over 95% high energy efficiency at a relatively low electric field of 140 MV/m, in nanocomposites consisting of ferroelectric $BaTiO_3$ filler embedded in a polymer matrix [21].

Interestingly, using an atomistic effective Hamiltonian simulations, different phases were predicted in ferroelectric nanocomposites consisting of periodic arrays of $BaTiO_3$ nanowires embedded in a $SrTiO_3$ matrix, for different temperature regions [22]. Some of these phases have a coupled macroscopic polarization and an electrical toroidal moment associated with vortices at low and intermediate temperatures [23], while heating the system leads to the progressive disappearance of the polarization and then vortices (note that frustration and ordering of topological defects were also found there [24]). One may therefore wonder how these phases, as well as the coupling between polarization and electrical toroidal moment, affect energy storage properties in ferroelectric nanocomposites. Also, can these properties be large? Is it also possible develop a simple model to analyze and explain their energy density, which may help in designing future ferroelectric nanocomposite systems with large energy storage performance?

*zjjiang@xjtu.edu.cn
†laurent@uark.edu

The aim of this paper is to address all the aforementioned important issues by conducting atomistic first-principles-based effective Hamiltonian simulations and interpreting the energy storage results via a phenomenological model. Such simulations and phenomenological model allow us to obtain a deep insight into energy storage properties of nanostructures. In particular, ultrahigh-energy densities (up to 141.2 J/cm^3) with an ideal efficiency of 100% is presently found. We also demonstrate that the energy density of ferroelectric nanocomposites can be decomposed into three energy contributions, each associated with a different behavior as a function of temperature for different equilibrium phases. This paper is organized as follows. Section II describes details about the effective Hamiltonian scheme used here. Results are presented in Sec. III. Finally, a summary is provided in Sec. IV.

II. METHODS

Here, we use the first-principles-based effective Hamiltonian (H_{eff}) approach developed in Ref. [25], with the total internal energy E_{int} being written as a sum of two main terms:

$$E_{\text{int}} = E_{\text{ave}}(\{\mathbf{u}_i\}, \{\eta_I\}, \{\eta_H\}) + E_{\text{loc}}(\{\mathbf{u}_i\}, \{\eta_I\}, \{\sigma_j\}, \{\eta_{\text{loc}}\}), \tag{1}$$

where the first energy term E_{ave} is associated with the local soft mode $\{\mathbf{u}_i\}$ in unit cell i (that is directly proportional to the electric dipole moment centered on Ti site i), and on the $\{\eta_I\}$ and $\{\eta_H\}$ inhomogeneous and homogeneous strain tensors, respectively. E_{ave} consists of five energetic parts: (i) a local mode self-energy; (ii) the long-range dipole-dipole interaction; (iii) short-range interactions between local soft modes; (iv) an elastic energy; and (v) interactions between local modes and strains [26]. The second energy term, E_{loc}, involves the $\{\sigma_j\}$ and $\{\eta_{\text{loc}}\}$ parameters. $\{\sigma_j\}$ characterizes the atomic configuration of the A sublattice, that is, $\sigma_j = +1$, or -1 corresponds to the distribution of Ba or Sr ions located at the j sites of the A sublattice in $(Ba_xSr_{1-x})TiO_3$ systems, respectively. $\{\eta_{\text{loc}}\}$ represents the local strain stemming from the difference in ionic radii between Ba and Sr atoms (that is, relatively large $\simeq$2%). We presently employ this effective Hamiltonian scheme within Monte Carlo (MC) simulations and large supercells to obtain energy storage properties in a ferroelectric $BaTiO_3$-$SrTiO_3$ nanocomposite. Note that E_{int} of Eq. (1) is used in MC simulations with the Metropolis algorithm [27], which allows us to compute finite-temperature properties of ferroelectric nanocomposites. Note also that E_{loc} of Eq. (1) automatically implied that intrinsic effects of the interface on physical properties (such as local electric dipoles and local strains) are accounted for. On the other hand, the role of structural defects such as dislocations are not included.

Practically, we consider a ferroelectric nanocomposite system made of a periodic square array of $BaTiO_3$ (BTO) nanowires embedded in a $SrTiO_3$ (STO) medium [22]. Figure 1 shows the considered nanocomposite structure used in this study. Note that each wire of this nanocomposite has a 4.8×4.8 nm^2 (144 sites of BTO) rectangular (x, y) cross section and a long axis running along the z axis (x, y, and z axes are parallel to the pseudocubic [100], [010], and [001] directions, respectively). Adjacent wires are separated by six sites ($\simeq$2.4 nm) of $SrTiO_3$ medium. This nanocomposite is mimicked by a 36×36×6 supercell (that contain 38 880 atoms), with a periodicity of six sites ($\simeq$2.4 nm) along the z axis.

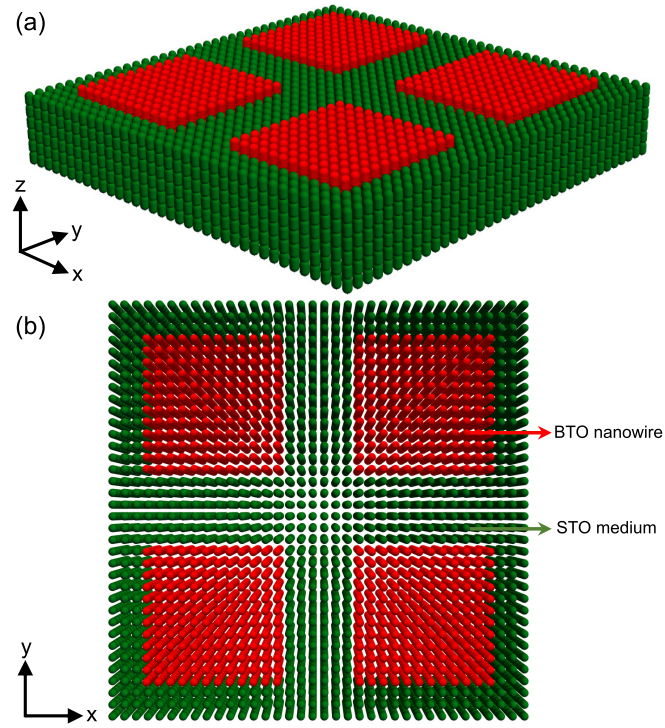

FIG. 1. Schematic representation of the 36×36×6 supercell mimicking the studied nanocomposite. (a) The structure is comprised of four $BaTiO_3$ nanowires (red color), with each one having a cross section of 12×12 (144 Ti sites) along the x and y directions separated by six sites of $SrTiO_3$ medium (green tubes), with a periodicity of six Ti sites along the z axis ([001] pseudocubic direction). (b) The top view of the ferroelectric nanocomposite supercell.

To mimic the energy storage properties under an applied dc electric field, an additional term $-\sum_i \mathbf{p}_i \cdot \mathcal{E}$ is added to the total internal energy E_{int}, where $\mathbf{p}_i$ is the local electric dipole (which is equal to the product between the local soft mode $\mathbf{u}_i$ and its Born effective charge Z^*) and $\mathcal{E}$ is the electric field that is applied along the z axis. To obtain converged results, 20 000 MC sweeps are run for equilibration and an additional 20 000 MC sweeps are used to get the statistical thermal averages at each considered temperature and applied electric field. Note that we numerically found that the theoretical electric field is larger from the measured one by a factor of 1.3 in $(Ba_xSr_{1-x})TiO_3$ compounds, by comparing the H_{eff}-obtained P-$\mathcal{E}$ loop with the experimental one for disordered $(Ba_{0.5}Sr_{0.5})TiO_3$ solid solutions at 300 K [28]. To correct for such discrepancy, the electric fields considered in the present paper are divided by a factor of 1.3. Figure 2 shows the resulting renormalized P-$\mathcal{E}$ loop of the disordered $(Ba_{0.5}Sr_{0.5})TiO_3$ system at room temperature, which matches the experimental one rather well. Note that such rescaling is an approach that has been previously successful in several compounds [9,14,16,29].

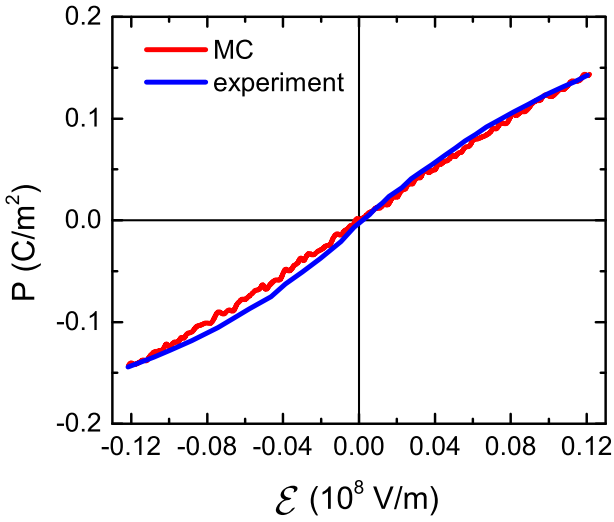

FIG. 2. P-$\mathcal{E}$ hysteresis loops obtained from MC data and from measurements in $(Ba_{0.5}Sr_{0.5})TiO_3$ system at 300 K (note that the theoretical electric field has been divided by a factor of 1.3).

III. RESULTS AND DISCUSSION

A. Different phases in the chosen $BaTiO_3$-$SrTiO_3$ nanocomposite

Figures 3(a)–3(h) show the temperature dependence of the overall and individual polarizations, the electrical toroidal moment, and the dipolar configurations in a given (x, y) plane for different temperatures in the chosen $BaTiO_3$-$SrTiO_3$ nanocomposite. The polarization contributions of BTO wires and STO medium to the total z-component polarization in Fig. 3(a) are given by $P_z(\text{BTO}) = a_{\text{lat}}Z^* \sum \mathbf{u}_{\text{BTO}}/NV$ and $P_z(\text{STO}) = a_{\text{lat}}Z^* \sum \mathbf{u}_{\text{STO}}/NV$, where a_{lat} is the five-atom lattice constant, Z^* represents the Born effective charge associated with the local mode, N is the number of sites in the supercell, V is the unit cell volume, and $\sum \mathbf{u}_{\text{BTO}}$ and $\sum \mathbf{u}_{\text{STO}}$ are the sum of the local modes centered on BTO wires and STO medium, respectively. Note that the electrical toroidal moment is defined as $\mathbf{G}_j = \frac{1}{2N_j}\sum_{i,j} \mathbf{r}_{i,j} \times \mathbf{p}_{i,j}$, where N_j is the number of sites in nanowire j; $\mathbf{p}_{i,j}$ is the local electrical dipole of site i in wire j, which is located at $\mathbf{r}_{i,j}$. A nonzero value of $\mathbf{G}_j$ typically characterizes dipole vortex in the nanowire j [30], and the data of Fig. 3(b) represents the average of these $\mathbf{G}_j$ over the four $BaTiO_3$ wires. Based on the evolutions of polarizations and toroidal moment versus temperature, six different phases are identified for this nanocomposite system. For instance, phase I exhibits a significant polarization and toroidal moment in BTO wires both along the pseudocubic [001] direction while the STO medium possesses vortices and antivortices, in addition to a polarization along [001] [see Fig. 3(c)]; phase II still has both vortices and polarization along the [001] direction in the BTO nanowire, and antivortices and polarization still occur in the STO medium. However, the z component of the dipoles in the STO medium is significantly reduced in phase II [see Figs. 3(a) and 3(d)]; in phase III, the polarization and vortices still appear in the BTO nanowires, but the vortices and antivortices in the STO medium have basically disappeared [see Fig. 3(e)]; phase IV distinguishes itself from phase III by the annihilation of the z component of the electrical dipoles in the STO medium [see Figs. 3(a) and 3(f)]. In phase V, the overall polarization vanishes, which indicates that the polarization disappears in both BTO wires and STO medium [see Fig. 3(a)]. However, the vortices still exist in the BTO nanowires in phase V [see Fig. 3(g)], as consistent with the nonzero z component of the electrical toroidal moment [see Fig. 3(b)]. The paraelectric and paratoroidic phase VI occurs above 330 K, where both the overall polarization and electrical toroidal moment have vanished [see Figs. 3(a), 3(b), and 3(h)]. Note that our predicted phases and their temperature range shown in Fig. 3 are in rather good agreement with previous theoretical findings [22] except for adding the (previously overlooked) new phase IV, where the polarization in the STO medium has disappeared. Note also that the temperatures at which successive changes in phases happen are 75, 125, 190, 240, and 330 K from phase I to phase VI, respectively, as emphasized in Figs. 3(a) and 3(b). To determine the boundaries between phases I–IV, we identified the temperatures at which the in-plane and out-of-plane dielectric responses peak below 240 K—as similar Ref. [22]. We also looked at the temperature dependence of electrical toroidal moment in the $BaTiO_3$ nanowires above 240 K to determine the boundary between phases V and VI.

B. Energy storage properties in the $BaTiO_3$-$SrTiO_3$ nanocomposite

To investigate the energy storage properties in the $BaTiO_3$-$SrTiO_3$ nanocomposite, a dc electric field $\mathcal{E}$ is applied along the pseudocubic [001] direction (z axis). Figure 4(a) displays the response of the z component of the overall polarization when the electric field increases from zero to $\mathcal{E}_{\text{max}} = 4.5\times10^8$ V/m for different temperatures. We also numerically find that the charging and discharging processes are completely reversible (note that the charging and discharging correspond to the processes of increasing the electric field from zero to the maximum applied field and then decreasing the field back to zero, respectively) for any considered temperature. The resulting efficiency is therefore 100%, which has also been reported in epitaxial AlN/ScN superlattices [16] and lead-free Ba(Zr, Ti)O_3 relaxor ferroelectrics [14] because these two latter compounds possess a field-induced *second-order* transition from an overall paraelectric to ferroelectric state. Figure 4(b) shows the electric field as a function of polarization for the same temperatures than those indicated in Fig. 4(a), which allows us to extract the energy density $U = \int_{P_r}^{P_{\text{max}}} \mathcal{E}dP$ by integrating the area below the $\mathcal{E}$-versus-P curve. Such kind of procedure can be done for any temperature and for any $\mathcal{E}_{\text{max}}$. Figure 4(c) displays the resulting energy density as a function of temperature, when choosing three maximal applied electric field $\mathcal{E}_{\text{max}}$: 4.5×10^8, 6.4×10^8, and 10×10^8 V/m. Note that a field of 4.5×10^8 V/m has been experimentally realized in $Ba_{0.2}Sr_{0.8}TiO_3$ nanocomposites [19], 6.4×10^8 V/m has been reached for the commercial polypropylene capacitors [6], and a field of 10×10^8 V/m was reported in $La_{0.1}Bi_{0.9}MnO_3$ and $BaTiO_3$ films [31,32]. As shown in Fig. 4(c), the energy density is only slightly

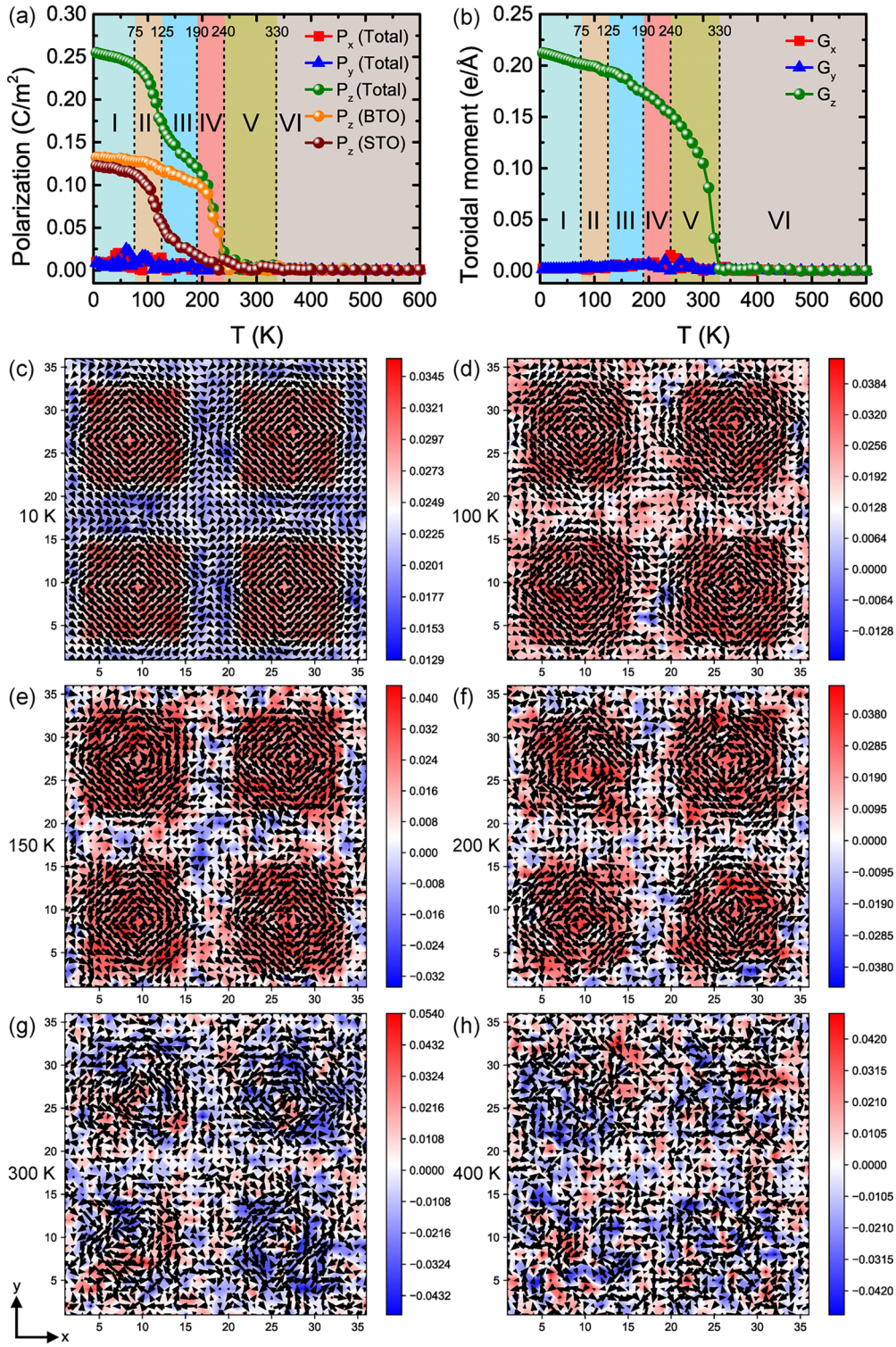

FIG. 3. Temperature dependence of some properties in the studied $BaTiO_3$-$SrTiO_3$ nanocomposite: (a) the macroscopic polarization, as well as the contribution of the z component of the polarization in the $BaTiO_3$ wires and $SrTiO_3$ medium to the overall polarization; (b) the average electrical toroidal moment in the $BaTiO_3$ nanowires; and (c)–(h) snapshots of dipolar configurations in a given (x, y) plane at 10 K (phase I), 100 K (phase II), 150 K (phase III), 200 K (phase IV), 300 K (phase V), and 400 K (phase VI) under zero electric field, respectively. The color bars indicate the magnitude of the out-of-plane component of the local modes.

temperature dependent and is nonlinear below 240 K (these temperatures correspond to the polar phases I–IV). It is equal to 38.3, 58.7, and 105.1 J/cm^3 at 240 K when the maximal applied fields are 4.5×10^8, 6.4×10^8, and 10×10^8 V/m, respectively. On the other hand, when the temperature is between 240 and 600 K (which is the range associated with phases V and VI), the energy density significantly and more linearly increases with

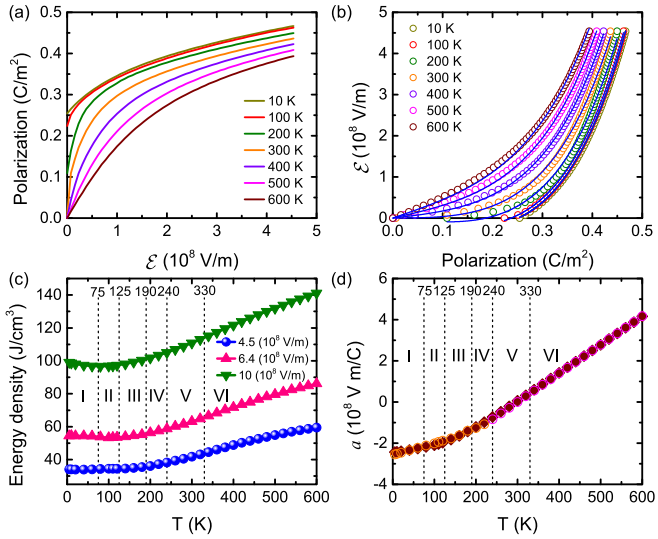

FIG. 4. (a) P-$\mathcal{E}$ curves at different selected temperatures obtained from MC simulations for electric field applied along the pseudocubic [001] direction. (b) Electric field versus polarization at these different temperatures in $BaTiO_3$-$SrTiO_3$ nanocomposite. The solid blue lines represent the fit of the MC $\mathcal{E}$-P data by Eq. (3). (c) Energy density obtained from MC simulation data versus temperature for electric fields applied along the pseudocubic [001] direction, with maximal applied electric fields of $\mathcal{E}_{max} = 4.5\times10^8$, 6.4×10^8, and 10×10^8 V/m, respectively. (d) Fitting parameter a of Eq. (3) as a function of temperature when the maximal applied electric field is equal to 4.5×10^8 V/m.

temperature, which provides values up to 59.5, 86.1, and 141.2 J/cm^3 for $\mathcal{E}_{max} = 4.5\times10^8$, 6.4×10^8, and 10×10^8 V/m, respectively. Strikingly, the predicted energy densities in the studied $BaTiO_3$-$SrTiO_3$ nanocomposite therefore exceed the experimentally value of 14.86 J/cm^3 reported for a maximum electric field of 4.5×10^8 V/m in $Ba_{0.2}Sr_{0.8}TiO_3$ nanowires [19], and is also much larger than the energy density of 1.2 J/cm^3 achieved in a commercial capacitor with a maximal field of 6.4×10^8 V/m [6].

To understand the energy density behaviors depicted in Fig. 4(c), one can use the following simple Landau-type free energy potential:

$$F = \tfrac{1}{2}a_0P^2 + \tfrac{1}{4}bP^4 + \tfrac{1}{6}cP^6 + \tfrac{1}{2}dP^2G^2 - \mathcal{E}P, \qquad (2)$$

where a_0, b, c, are coefficients that correspond to quadratic, quartic, sextic coefficients, respectively, while d quantifies the sign and strength of the biquadratic coupling between the polarization and electrical toroidal moment.

Under equilibrium conditions, the polarization P satisfies $\frac{\partial F}{\partial P} = 0$, which yields

$$\mathcal{E} = (a_0 + dG^2)P + bP^3 + cP^5 = aP + bP^3 + cP^5, \qquad (3)$$

where $a = a_0 + dG^2$.

As shown in Fig. 4(b), the electric field versus polarization ($\mathcal{E}$-P) data obtained from MC simulations for all considered temperatures can be relatively well fitted by the rather simple Eq. (3) (see solid blue lines), taking the total polarization from Fig. 3(a) and allowing a to be a free parameter while b and c are constant for any temperature (as consistent with traditional Landau theories). Such good fitting confirms the validity of our present Landau model, and also results in the determination of the b and c coefficients as well as the temperature behavior of a. This latter is shown in Fig. 4(d) for the maximal field $\mathcal{E}_{max} = 4.5\times10^8$ V/m applied along the [001] pseudocubic direction. Moreover, this fitting also provides values of the b and c parameters to be 30.9×10^8 V m^5/C^3 and 114.2×10^8 V m^9/C^5, respectively.

We will comment on the temperature behavior of the a coefficient soon, but let us first recall that the recoverable energy density can be written as $U = \int_{P_r}^{P_{max}} \mathcal{E}dP$, which, when inserting Eq. (3), gives

$$\begin{aligned} U &= \int_{P_r}^{P_{max}} (aP + bP^3 + cP^5)dP \\ &= \frac{1}{2}a\left(P_{max}^2 - P_r^2\right) + \frac{1}{4}b\left(P_{max}^4 - P_r^4\right) + \frac{1}{6}c\left(P_{max}^6 - P_r^6\right), \end{aligned} \qquad (4)$$

where P_{max} is the maximum polarization at $\mathcal{E}_{max}$ and P_r is the remnant polarization. Equation (4) therefore tells us that U is a rather straightforward function of a, b, c, P_r, and P_{max}. Note that P_r is directly obtainable from the MC data and is nonzero for temperatures between 5 and 240 K (which covers the ranges of phases I, II, III, and IV) while it vanishes for temperatures above 240 K (corresponding to phases V and VI) as shown in Figs. 3(a) and 4(a). Note also that P_{max} can either be directly obtained from the MC simulations by taking the value of the polarization at $\mathcal{E}_{max}$ or computed via Eq. (3) at this considered $\mathcal{E}_{max}$ and using the MC-fitted parameters of a, b, and c. As we are going to see, both procedures give similar results.

Let us now comment on the a coefficient. Figure 4(d) shows that the fitting parameter a has a nonlinear behavior for temperatures below 240 K and then basically linearly increases with temperature between 240 and 600 K, at $\mathcal{E}_{max} = 4.5\times10^8$ V/m. For instance, the a parameter decreases its magnitude from -2.44×10^8 to -0.73×10^8 V m/C in a nonlinear fashion between 5 and 240 K, then linearly decreases in magnitude with temperature between 240 and 600 K up to 4.16×10^8 V m/C—with a being equal to zero at 300 K. Note that, as shown by open circles symbol of Fig. 4(d), the fitting parameter a can be well fitted by $a_1(T_c - T) + dG^2$ in the polar phases I–IV below 240 K with T_c being equal to 300 K and the toroidal moment being the one shown in Fig. 3(b). The resulting a_1 is -4.5×10^5 V m/C K while $d = 183.4$ V Å$^3/e^3$. The positive sign of d therefore indicates a competition between polarization and toroidal moment, which also explains why the fitting provides a T_c of 300 K, while the true Curie temperature of the studied nanocomposite is lower and equal to 240 K. Moreover and as also shown by open circles symbols in Fig. 4(d), a can further be well fitted by $a = a_2(T - T_c)$ in region V (for which the polarization has vanished but the toroidal moment still exists) and region VI (for which the total polarization and toroidal moment have both been annihilated), with T_c being equal to 300 K too. Note that the fitted a_2 is 1.4×10^6 V m/C K and that these different behaviors and analytical formula of a for temperatures below versus above 240 K are consistent with the general line indicated below Eq. (3), namely,

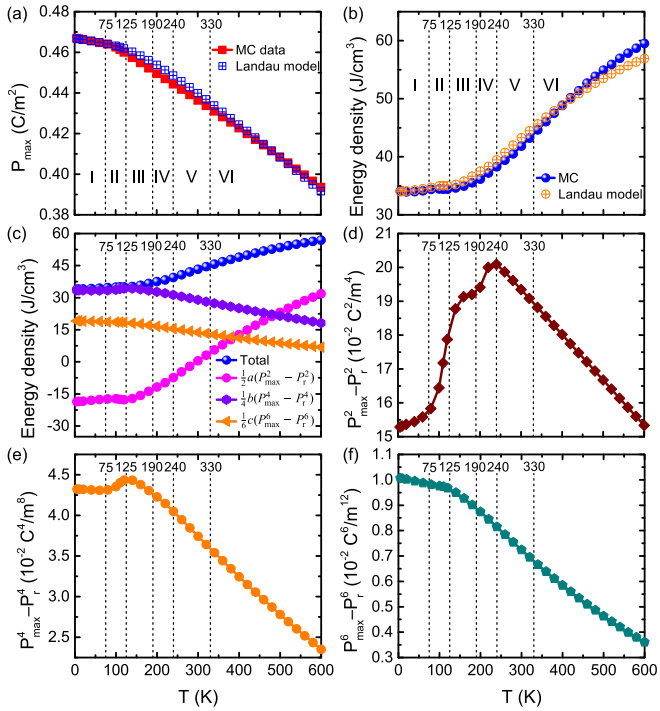

FIG. 5. (a) The maximum polarization P_{max} obtained from MC simulations and Landau model [see Eq. (3)] as a function of temperature for $\mathcal{E}_{max} = 4.5\times10^8$ V/m and fields applied along the [001] direction in the studied $BaTiO_3$-$SrTiO_3$ nanocomposite. (b) Energy density obtained from MC simulations and Eq. (4) as a function of temperature for a maximal applied electric field $\mathcal{E}_{max} = 4.5\times10^8$ V/m. (c) The total and decomposed energy densities $\frac{1}{2}a(P^2_{max} - P^2_r)$, $\frac{1}{4}b(P^4_{max} - P^4_r)$, and $\frac{1}{6}c(P^6_{max} - P^6_r)$ obtained from Eq. (4) as a function of temperature for $\mathcal{E}_{max} = 4.5\times10^8$ V/m. (d)–(f) $P^2_{max} - P^2_r$, $P^4_{max} - P^4_r$, and $P^6_{max} - P^6_r$ versus temperature for $\mathcal{E}_{max} = 4.5\times10^8$ V/m, respectively.

that $a = a_0 + dG^2$—with a_0 being directly proportional to $(T - T_c)$, as consistent with typical Landau theory, and with d being finite when both spontaneous polarization and toroidal moment exist and zero otherwise.

Furthermore, Fig. 5(a) displays the value of the maximum polarization, P_{max} as a function of temperature both from MC simulations and from the Landau model using the MC-fitted parameters of a, b, and c in Eq. (3). One can clearly see that for all considered temperatures at $\mathcal{E}_{max} = 4.5\times10^8$ V/m, the MC simulations and the Landau-model-obtained P_{max} provide nearly similar results, which is quite remarkable once realizing the simplicity of Eq. (3), on one hand, and the complexity of the investigated system on the other hand. As shown in Fig. 5(a), P_{max} almost linearly and very slightly decreases with temperature in regions I and II for temperatures between 5 and 125 K (values varying between 0.467 to 0.460 C/m^2). In regions III–VI for temperatures ranging between 125 and 600 K, P_{max} basically linearly decreases in a more significant fashion with temperature (the value of P_{max} varies from 0.460 to 0.394 C/m^2).

To understand the energy density results in Fig. 4(c), we take advantage of Eq. (4). Figure 5(b) shows the energy density directly obtained from Eq. (4) at the maximal applied field of $\mathcal{E}_{max} = 4.5\times10^8$ V/m, along with the energy density data computed from the MC simulations. The Landau-model-obtained energy density agrees reasonably well with the MC-obtained energy density. Moreover, and according to Eq. (4), the energy density is the sum of three terms, which are $\frac{1}{2}a(P^2_{max} - P^2_r)$, $\frac{1}{4}b(P^4_{max} - P^4_r)$, and $\frac{1}{6}c(P^6_{max} - P^6_r)$. The three contributions of energy density are shown in Fig. 5(c), while Figs. 5(d)–5(f) display the temperature dependency of $(P^2_{max} - P^2_r)$, $(P^4_{max} - P^4_r)$, and $(P^6_{max} - P^6_r)$, respectively. The first contribution of the energy density thus relies on the product of the a parameter and $P^2_{max} - P^2_r$, and only slightly depends on temperature with a nonlinear behavior in regions I and II for temperatures between 5 and 125 K (the energy density value associated with this first term ranges from -18.6 to -17.7 J/cm^3 within phases I and II). This first energy density term of $\frac{1}{2}a(P^2_{max} - P^2_r)$ is almost constant in this temperature range because there is a compensation between the facts that (the negative) a decreases in magnitude and that $P^2_{max} - P^2_r$ increases with temperature. On the other hand, such compensation does not occur anymore for temperatures from 125 to 240 K (from phase III to phase IV) due to the strong nonlinear increase of $P^2_{max} - P^2_r$ as well as the more pronounced (nonlinear) decrease of the magnitude of a. Consequently, the first energy density term, $\frac{1}{2}a(P^2_{max} - P^2_r)$, almost linearly increases with temperature between 125 and 240 K. In phases V and VI (for temperatures between 240 and 600 K), a linearly increases with temperature (from -0.73×10^8 to 4.16×10^8 V m/C) faster than $P^2_{max} - P^2_r$ decreases with temperature (from 0.201 to 0.153 C^2/m^4), hence resulting in $\frac{1}{2}a(P^2_{max} - P^2_r)$ increasing in a linear fashion with temperature.

The second contribution of energy density, $\frac{1}{4}b(P^4_{max} - P^4_r)$, is only slightly dependent on temperature between 5 and 125 K (the values varying between 33.4 and 34.3 J/cm^3) because $P^4_{max} - P^4_r$ is basically constant (around 0.043 C^4/m^8) there and b is always a constant in our fitting. Above 125 K (from region III to region VI), $\frac{1}{4}b(P^4_{max} - P^4_r)$ linearly decreases with temperature up to 600 K (from 34.3 at 125 K to 18.2 J/cm^3 at 600 K) because $P^4_{max} - P^4_r$ adopts such behavior (it decreases from 0.044 to 0.024 C^4/m^8).

The third energy density, $\frac{1}{6}c(P^6_{max} - P^6_r)$, only very slightly decreases with temperature in phases I and II, i.e., for temperatures ranging between 5 and 125 K, which arises from the weak decrease of $P^6_{max} - P^6_r$ (from 0.0101 C^6/m^{12} at 5 K to 0.0097 C^6/m^{12} at 125 K) in these regions—since the c parameter is constant too. Furthermore, for temperatures ranging between 125 and 600 K (in regions III–VI), $\frac{1}{6}c(P^6_{max} - P^6_r)$ rather strongly and continuously decreases with temperature up to 600 K (from 18.4 to 6.9 J/cm^3) as a result of the significant decrease of $P^6_{max} - P^6_r$ with temperature from 0.0097 to 0.0036 C^6/m^{12}.

Figure 5(c) further shows that the energy densities of $\frac{1}{2}a(P^2_{max} - P^2_r)$ and $\frac{1}{6}c(P^6_{max} - P^6_r)$ nearly cancel each other in phases I and II for temperatures ranging between 5 and 125 K, implying that $\frac{1}{4}b(P^4_{max} - P^4_r)$ is the dominant contribution there—which also explains why the total energy density only very slightly depends on temperatures in these regions. In phases III and IV, the first energy density $\frac{1}{2}a(P^2_{max} - P^2_r)$ increases with temperature while the second and third energy

densities both decrease, which, once again, results in a total energy density that only weakly depends on temperature. On the other hand, in phases V and VI, the total energy density is significantly enhanced with temperature, and in a nearly linear fashion, following the strong linear increase of $\frac{1}{2}a(P_{\rm max}^2 - P_{\rm r}^2)$ which is counteracted by the smaller linear decrease of the second and third energy densities. Interestingly, the contributions in percentage of the total energy density can be temperature dependent between regions V and VI. As a matter of fact, the contributions of $\frac{1}{2}a(P_{\rm max}^2 - P_{\rm r}^2)$, $\frac{1}{4}b(P_{\rm max}^4 - P_{\rm r}^4)$ and $\frac{1}{6}c(P_{\rm max}^6 - P_{\rm r}^6)$ to the total energy density at 300 K are 0%, 67%, and 33%, respectively (the zero value of the first energy term arises from the annihilation of a at 300 K). This is to be compared with the corresponding numbers of 56%, 32%, and 12%, respectively, at 600 K.

IV. SUMMARY

In conclusion, based on atomistic effective Hamiltonian scheme combined with MC simulations, we investigated the energy storage properties in a $BaTiO_3$-$SrTiO_3$ nanocomposite consisting of $BaTiO_3$ nanowires embedded in a $SrTiO_3$ matrix. We found that this nanocomposite system can exhibit large energy densities and an ideal 100% efficiency for three considered maximal applied electric fields. It is also found that the energy density-versus-temperature curve is nonlinear and only weakly dependent on temperature for temperatures below 240 K (for which the equilibrium phases are polar). On the other hand, it becomes more linear and strongly temperature dependent as the temperature increases from 240 to 600 K, when the system progressively loses its spontaneous polarization and then its spontaneous toroidal moment. Such unusual energy storage features are then interpreted via the development of a simple Landau model that reproduces the MC simulation data and that also involves a coupling between polarization and toroidal moment. In particular, the energy density consists of three energy terms, namely, $\frac{1}{2}a(P_{\rm max}^2 - P_{\rm r}^2)$, $\frac{1}{4}b(P_{\rm max}^4 - P_{\rm r}^4)$, and $\frac{1}{6}c(P_{\rm max}^6 - P_{\rm r}^6)$, that adopt different behaviors in different structural phases. The proposed phenomenological model may be further put in use to search for, or analyze results of, other ferroelectric nanostructures with large energy density.

ACKNOWLEDGMENTS

This work is supported by the National Natural Science Foundation of China (Grant No. 11804138), Natural Science Basic Research Program of Shaanxi (Program No. 2023-JC-YB-017), Shaanxi Fundamental Science Research Project for Mathematics and Physics (Grant No. 22JSQ013), "Young Talent Support Plan" of Xi'an Jiaotong University (Grant No. WL6J004), and the Fundamental Research Funds for the Central Universities. L.B. acknowledges ARO Grant No. W911NF-21-1-0113 and the Vannevar Bush Faculty Fellowship Grant No. N00014-20-1-2834 from the Department of Defense. The HPC Platform of Xi'an Jiaotong University is also acknowledged. This paper is dedicated to Professor Henry Krakauer, who made pioneering contributions to the understanding of ferroelectrics via the development and use of original numerical techniques.

[1] B. Chu, X. Zhou, K. Ren, B. Neese, M. Lin, Q. Wang, F. Bauer, and Q. M. Zhang, Science **313**, 334 (2006).
[2] Q. Li, L. Chen, M. R. Gadinski, S. Zhang, G. Zhang, H. U. Li, E. Iagodkine, A. Haque, L.-Q. Chen, T. N. Jackson, and Q. Wang, Nature (London) **523**, 576 (2015).
[3] Prateek, V. K. Thakur, and R. K. Gupta, Chem. Rev. **116**, 4260 (2016).
[4] H. Palneedi, M. Peddigari, G.-T. Hwang, D.-Y. Jeong, and J. Ryu, Adv. Funct. Mater. **28**, 1803665 (2018).
[5] L. Yang, X. Kong, F. Li, H. Hao, Z. Cheng, H. Liu, J.-F. Li, and S. Zhang, Prog. Mater. Sci. **102**, 72 (2019).
[6] M. Rabuffi and G. Picci, IEEE Trans. Plasma Sci. **30**, 1939 (2002).
[7] H. Pan, F. Li, Y. Liu, Q. Zhang, M. Wang, S. Lan, Y. Zheng, J. Ma, L. Gu, Y. Shen, P. Yu, S. Zhang, L.-Q. Chen, Y.-H. Lin, and C.-W. Nan, Science **365**, 578 (2019).
[8] B. Peng, Q. Zhang, X. Li, T. Sun, H. Fan, S. Ke, M. Ye, Y. Wang, W. Lu, H. Niu, J. F. Scott, X. Zeng, and H. Huang, Adv. Electron. Mater. **1**, 1500052 (2015).
[9] B. Xu, J. Íñiguez, and L. Bellaiche, Nat. Commun. **8**, 15682 (2017).
[10] Y. Zhang, L. Bellaiche, and B. Xu, Phys. Rev. Mater. **6**, L051401 (2022).
[11] A. A. Instan, S. P. Pavunny, M. K. Bhattarai, and R. S. Katiyar, Appl. Phys. Lett. **111**, 142903 (2017).
[12] J. Kim, S. Saremi, M. Acharya, G. Velarde, E. Parsonnet, P. Donahue, A. Qualls, D. Garcia, and L. W. Martin, Science **369**, 81 (2020).
[13] H. Pan, S. Lan, S. Xu, Q. Zhang, H. Yao, Y. Liu, F. Meng, E.-J. Guo, L. Gu, D. Yi, X. R. Wang, H. Huang, J. L. MacManus-Driscoll, L.-Q. Chen, K.-J. Jin, C.-W. Nan, and Y.-H. Lin, Science **374**, 100 (2021).
[14] Z. Jiang, S. Prosandeev, and L. Bellaiche, Phys. Rev. B **105**, 024102 (2022).
[15] H. Aramberri, N. S. Fedorova, and J. Íñiguez, Sci. Adv. **8**, eabn4880 (2022).
[16] Z. Jiang, B. Xu, H. Xiang, and L. Bellaiche, Phys. Rev. Mater. **5**, L072401 (2021).
[17] C. Hou, W. Huang, W. Zhao, D. Zhang, Y. Yin, and X. Li, ACS Appl. Mater. Interfaces **9**, 20484 (2017).
[18] J. Li, S. I. Seok, B. Chu, F. Dogan, Q. Zhang, and Q. Wang, Adv. Mater. **21**, 217 (2009).
[19] H. Tang and H. A. Sodano, Nano Lett. **13**, 1373 (2013).
[20] X. Huang and P. Jiang, Adv. Mater. **27**, 546 (2015).
[21] Z. Liu, B. Yang, W. Cao, E. Fohtung, and T. Lookman, Phys. Rev. Appl. **8**, 034014 (2017).
[22] L. Louis, I. Kornev, G. Geneste, B. Dkhil, and L. Bellaiche, J. Phys.: Condens. Matter **24**, 402201 (2012).
[23] S. Prosandeev, A. Malashevich, Z. Gui, L. Louis, R. Walter, I. Souza, and L. Bellaiche, Phys. Rev. B **87**, 195111 (2013).

[24] Y. Nahas, S. Prokhorenko, and L. Bellaiche, Phys. Rev. Lett. **116**, 117603 (2016).
[25] L. Walizer, S. Lisenkov, and L. Bellaiche, Phys. Rev. B **73**, 144105 (2006).
[26] W. Zhong, D. Vanderbilt, and K. M. Rabe, Phys. Rev. B **52**, 6301 (1995).
[27] N. Metropolis, A. W. Rosenbluth, M. N. Rosenbluth, A. H. Teller, and E. Teller, J. Chem. Phys. **21**, 1087 (1953).
[28] X. Lu, Y. Tong, H. Talebinezhad, L. Zhang, and Z.-Y. Cheng, J. Alloys Compd. **745**, 127 (2018).
[29] Z. Jiang, Y. Nahas, S. Prokhorenko, S. Prosandeev, D. Wang, J. Iñiguez, and L. Bellaiche, Phys. Rev. B **97**, 104110 (2018).
[30] I. I. Naumov, L. Bellaiche, and H. Fu, Nature (London) **432**, 737 (2004).
[31] M. Gajek, M. Bibes, S. Fusil, K. Bouzehouane, J. Fontcuberta, A. Barthélémy, and A. Fert, Nat. Mater. **6**, 296 (2007).
[32] V. Garcia, S. Fusil, K. Bouzehouane, S. Enouz-Vedrenne, N. D. Mathur, A. Barthélémy, and M. Bibes, Nature (London) **460**, 81 (2009).